Physics-Constrained Kalman Filtering for Wheel Normal Load Estimation Using Suspension and IMU Measurements

Angus Siegloff and Kyunghwan Choi, *Member, IEEE*

***Abstract*—This paper presents a physics-constrained Kalman filtering approach for estimating individual wheel normal loads using suspension and inertial measurement unit (IMU) measurements. The proposed method combines suspension-based wheel-load pseudo-measurements with IMU-based rigid-body equilibrium relations. These relations, including vertical-force, pitch-moment, and roll-moment equilibrium, are incorporated as probabilistic physical constraints, enabling the estimator to retain local sensitivity to suspension-induced load variations while enforcing global physical consistency in the wheel-load distribution. Spring, asymmetric damper, anti-roll-bar, and aerodynamic effects are included to improve the fidelity of the pseudo-measurements and constraints. The method is validated in IPG CarMaker under diverse driving scenarios, including the ISO double lane change, Nürburgring, and Hockenheim, and is compared with algebraic, quasi-static, suspension-only, and literature-based observer methods. The results demonstrate that the proposed method provides the most consistent overall performance across transient and full-lap conditions, while ablation studies confirm the dominant role of the physics-based constraint update in robust estimation.**

***Index Terms*—Wheel normal load estimation, physics-constrained Kalman filtering, vehicle dynamics, suspension modeling, state estimation.**

I. Introduction

ACCURATE estimation of individual wheel normal loads is essential in vehicle dynamics because tire-road friction potential, and thus the achievable longitudinal and lateral tire forces, depends directly on vertical loading. Reliable wheel-load information is therefore important for braking, traction and stability control, rollover prevention, and advanced chassis control systems. This importance is reflected in recent studies on vehicle state and parameter estimation, where accurate force and friction information supports vehicle stability assessment [1], sideslip and state reconstruction [2], and integrated vehicle dynamics control [3]. Related work on tire-road friction estimation further underscores the role of wheel normal load estimation as a prerequisite for reliable tire-force estimation and vehicle control [4], [5]. Direct measurement using wheel force transducers, however, is generally impractical for production vehicles because of cost, durability, and packaging limitations. Consequently, wheel normal loads are typically estimated from standard onboard sensors.

*This work was supported by the National Research Foundation of Korea (NRF) grant funded by the Korea government (MSIT) (RS-2025-00554087).

Angus Siegloff is with the Institute of Innovation, Science and Sustainability, Federation University, Mt Helen, Australia (e-mail: asiegloff@students.federation.edu.au).

Kyunghwan Choi is with Cho Chun Shik Graduate School of Mobility, Korea Advanced Institute of Science and Technology, Daejeon, Republic of Korea (e-mail: kh.choi@kaist.ac.kr).

Observer-based approaches, particularly Kalman-filter-based methods, have been widely studied for production-oriented wheel-load estimation. Early studies showed that body accelerations and suspension measurements can be used to estimate vertical tire forces [6], [7], and later works improved estimation fidelity by considering road grade, suspension sensing, and coupled vehicle-state estimation [8]–[10]. Related work on online grip and tire-force estimation has also emphasized the importance of combining physical modeling with estimator design for real-time vehicle-dynamics functions [11]. Beyond control-oriented applications, accurate wheel normal load estimation can also support ride comfort and safety by improving the rejection of road-induced disturbances and the use of available tire friction [12]. These requirements are challenging because wheel normal loads contain both suspension-driven high-frequency components associated with road excitation and lower-frequency components associated with inertial load transfer during vehicle maneuvers. Practical estimators should therefore retain local sensitivity to suspension-induced load variations while maintaining globally consistent load distribution at the vehicle level.

Several representative directions have been explored to reconstruct wheel normal loads from available vehicle signals, but they differ in how they use suspension-side information, vehicle-level dynamics, and additional modeling assumptions. Cascaded Kalman filter structures often estimate additional forces or vehicle states together with wheel normal loads [13], [14]. These approaches provide a systematic stochastic estimation framework, but they often rely on simplified suspension models, such as linear spring-damper representations, which can limit accuracy when anti-roll-bar coupling, bump-stop engagement, or damper asymmetry significantly affects load distribution. Rigid-body-equilibrium-based methods provide another direction. For example, the heuristic method of [15] reconstructs individual wheel loads using vertical force and moment balance without explicitly estimating tire forces through a stochastic observer. Controller output observers have also been developed using half-car or quarter-car formulations [16], [17]. While the approaches in [15]–[17] reduce reliance on direct force measurements, their practical applicability can be limited by assumptions introduced in the underlying vehicle or road models, such as simplified road conditions, reduced-order suspension descriptions, or operating-condition constraints.

More recently, data-driven, hybrid, and intelligent-tire-based approaches have been investigated to capture nonlinearities that are difficult to model analytically. Neural-network-based methods have been combined with maneuver classification for normal-load estimation under noisy conditions [18], and recent

tire-force estimation studies have explored model-based and machine-learning combinations [19] as well as purely data-driven frameworks for autonomous driving applications [20]. Intelligent-tire-based approaches infer vertical or combined tire forces from internal tire sensing [21]–[24]. Although promising, these methods often require specialized sensors, adaptation procedures, or extensive training data, which can restrict their deployment in standard production vehicles.

Despite these advances, two limitations remain. First, existing methods have not fully resolved the balance between local suspension sensitivity and global vehicle-level physical consistency in wheel normal load estimation. Suspension-model-based approaches can capture wheel-level load variations induced by suspension motion and road excitation, but their suspension models often remain simplified and may not explicitly account for vehicle-level force and moment consistency. Conversely, rigid-body or quasi-static formulations can represent vehicle-level load transfer through force and moment balance, but often lack sensitivity to local suspension-induced load variations. Second, comparative validation is often limited to selected maneuvers or a narrow set of baseline methods, making it difficult to assess robustness under diverse and realistic driving conditions.

To address these limitations, this paper proposes a physics-constrained Kalman filtering framework for estimating individual wheel normal loads using suspension and inertial measurement unit (IMU) measurements. The proposed method treats the four wheel normal loads as filter states and converts suspension displacement and velocity signals into wheel-load pseudo-measurements using spring, asymmetric damper, and anti-roll-bar force models, thereby providing local wheel-level sensitivity. IMU-based vertical-force, pitch-moment, and roll-moment equilibrium relations are then used to provide global vehicle-level consistency. Building on constrained Kalman filtering, which provides a principled way to incorporate physical relations into recursive state estimation [25]–[29], these equilibrium relations are introduced as soft probabilistic physical constraints. This formulation allows the estimator to retain local sensitivity to suspension-induced load variations while enforcing global physical consistency in the wheel-load distribution. An aerodynamic vertical-load correction is also included in the equilibrium relations to reduce speed-dependent bias at higher vehicle speeds.

The main contributions of this paper are represented in Fig. 1 and summarized as follows:

- **Physics-constrained Kalman filtering framework**: A two-stage estimator that combines suspension-based wheel-load pseudo-measurements with IMU-based rigid-body equilibrium relations, retaining local suspension sensitivity while enforcing global physical consistency in the wheel-load distribution.
- **Improved suspension-based pseudo-measurement construction**: Inclusion of spring, asymmetric damper, and anti-roll-bar effects to improve the fidelity of local wheel-level force information, while preserving a modular structure that allows the suspension-side model to be refined without altering the filter formulation.

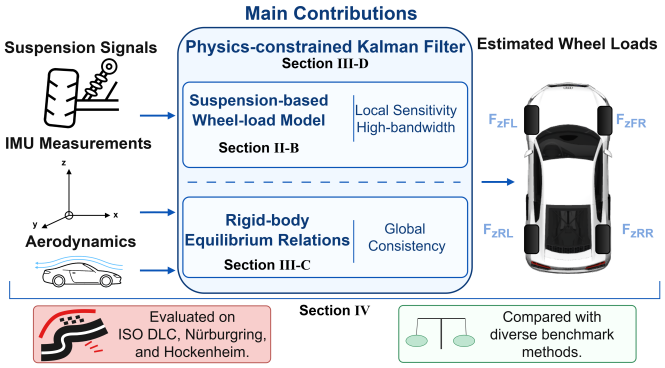

Fig. 1. Main contributions diagram.

- **Aerodynamic vertical-load correction**: Inclusion of aerodynamic vertical loading in the equilibrium relations to reduce speed-dependent estimation bias at higher vehicle speeds.
- **Broad comparative validation**: Evaluation against algebraic, quasi-static, suspension-only, and literature-based observer methods in the ISO double lane change, Nürburgring, and Hockenheim scenarios, demonstrating consistent performance across transient and full-lap conditions.

The remainder of this paper is organized as follows. Section II presents the suspension-based wheel-load model, which is used to construct wheel-load pseudo-measurements. Section III introduces the IMU-based rigid-body equilibrium relations and describes the proposed physics-constrained Kalman filtering framework that combines these relations with the suspension-based pseudo-measurements. Section IV presents the simulation validation and comparative performance analysis. Finally, Section V concludes the paper.

II. Suspension-Based Wheel-Load Model

This section develops the suspension-based wheel-load model used in the proposed estimator. The objective is twofold. First, conventional suspension models used in wheel-load estimation are extended to better capture wheel-level load generation mechanisms, including axle coupling and selected asymmetric or nonlinear effects. Second, the resulting suspension-based wheel-load estimates are used as pseudo-measurements in the Kalman filtering framework, providing local wheel-level force information that complements the global rigid-body equilibrium relations introduced in Section III.

A. Conventional suspension modeling

A useful conceptual starting point for vertical vehicle dynamics is the classical quarter-car model, in which a sprung mass is supported by a passive spring and damper [30]. For base excitation, the force transmitted through the suspension element may be written as

$$F_{\mathrm{qc}} = k\,(z_s - z_r) + c\,(\dot{z}_s - \dot{z}_r), \tag{1}$$

where z_s is the sprung-mass vertical displacement, z_r is the road-induced base displacement, and k and c are the suspension stiffness and damping coefficients. The corresponding sprung-mass force balance is

$$m_s\,\ddot{z}_s + c\,(\dot{z}_s - \dot{z}_r) + k\,(z_s - z_r) = 0, \tag{2}$$

where m_s denotes the quarter-car sprung mass.

This representation is useful for interpretation, but it is not used directly in the estimator because the road displacement z_r is not measured and because the classical quarter-car form does not capture left-right coupling or nonlinear suspension behavior. In particular, passive anti-roll bars generate opposing wheel forces under differential left-right motion [31], while practical dampers often exhibit asymmetric compression and rebound characteristics. These effects motivate the wheel-level suspension model adopted below.

B. Proposed suspension-based wheel-load modeling

This subsection develops the proposed suspension-based wheel-load model used to construct local wheel-load information for the Kalman filtering framework. Building on conventional quarter-car and half-car suspension representations, the suspension-related contribution to the wheel normal load at each wheel is expressed as

$$F_{z,i}^{\mathrm{susp}} = F_{z,i}^{\mathrm{spr}}(d_i) + F_{z,i}^{\mathrm{dam}}(v_i) + F_{z,i}^{\mathrm{arb}}(\Delta\eta), \tag{3}$$

where $F_{z,i}^{\mathrm{spr}}$, $F_{z,i}^{\mathrm{dam}}$, and $F_{z,i}^{\mathrm{arb}}$ denote the spring, damper, and anti-roll-bar contributions at wheel i, respectively. The variables d_i and v_i denote the measured suspension compression and compression velocity, and $\Delta\eta$ denotes the effective left-right axle deflection driving the anti-roll bar. The wheel index is $i \in \{\mathrm{FL}, \mathrm{FR}, \mathrm{RL}, \mathrm{RR}\}$.

Unlike a classical quarter-car model, this formulation incorporates axle-level coupling through the anti-roll bar. It should therefore be interpreted as an effective wheel-level suspension-load model for constructing local wheel-load information rather than as a full multi-body suspension model. Unsprung-mass dynamics and tire compliance are neglected at this stage. The following subsections define the spring, damper, and anti-roll-bar force contributions used to construct the overall model.

1) Spring force: The elastic component of the model is represented by a linear spring law,

$$F_z^{\mathrm{spr}}(d) = k\,d, \tag{4}$$

where d is suspension compression and k is the axle-specific spring stiffness. This approximation captures the dominant elastic behavior over the normal operating range and keeps the model compact. At larger compression levels, the simulated suspension response may deviate from this model because of bump-stop engagement and other nonlinear effects that are not explicitly represented here.

Separate spring stiffness values are used for the front and rear axles to reflect their different suspension characteristics.

2) Damper force: Damper force is modeled as a piecewise-linear function of suspension velocity to account for the asymmetric behavior typically observed between compression and rebound:

$$F_z^{\mathrm{dam}}(v) = \begin{cases} c_{\mathrm{push}}\,v, & v \geq 0, \\ c_{\mathrm{pull}}\,v, & v < 0, \end{cases} \tag{5}$$

where $v > 0$ corresponds to compression. The coefficients c_{push} and c_{pull} are obtained from local linear fits to the low-velocity region of the damper force-velocity characteristic.

This simplified representation captures the dominant asymmetry of automotive dampers while maintaining numerical robustness and estimator compactness. Although real dampers may exhibit strongly nonlinear or digressive behavior at higher velocities, such effects can be incorporated through a more detailed map without altering the estimator structure.

3) Anti-roll bar force: The anti-roll bar (ARB) introduces axle-level coupling between the left and right suspension elements. When the two wheels of an axle experience different vertical displacements, the stabilizer bar generates opposing vertical force contributions at the left and right wheels. This effect is especially important during lateral maneuvers, where differential suspension motion contributes directly to left–right load redistribution [31].

For a generic axle, the ARB force contribution is modeled in terms of an equivalent differential ARB deformation, $\Delta\eta$, as

$$F_{z,L}^{\mathrm{arb}} = -k_{\mathrm{arb}}\,\Delta\eta, \qquad F_{z,R}^{\mathrm{arb}} = +k_{\mathrm{arb}}\,\Delta\eta, \tag{6}$$

where k_{arb} denotes the effective ARB stiffness. This sign convention preserves action-reaction across the axle and captures the dominant stabilizer-bar load-transfer effect.

In a real suspension, the equivalent ARB deformation is determined by the left and right suspension motions through the suspension linkage geometry. Therefore, rather than depending on a single suspension displacement, $\Delta\eta$ is generally a nonlinear function of both measured suspension compressions,

$$\Delta\eta = \Phi_{\mathrm{arb}}(d_L, d_R), \tag{7}$$

where d_L and d_R are the left and right suspension compressions, and $\Phi_{\mathrm{arb}}(\cdot)$ represents the geometry-dependent ARB deformation mapping.

Because the CarMaker configuration used in this study does not include a detailed ARB linkage-geometry representation, the equivalent differential ARB deformation is modeled using a constant axle-level mapping from the measured suspension compression difference:

$$\Delta\eta_a \approx \gamma_{\mathrm{arb},a}\left(d_{L(a)} - d_{R(a)}\right), \tag{8}$$

where $a \in \{f, r\}$ denotes the front or rear axle, and $L(a)$ and $R(a)$ denote the left and right wheels on that axle, respectively. The coefficient $\gamma_{\mathrm{arb},a}$ represents the effective axle-level mapping from suspension compression difference to equivalent ARB deformation. Substituting (8) into (6) yields the ARB force contribution used in the suspension-load model. This term introduces the required left-right axle coupling using the measured suspension compression difference, while any residual discrepancy relative to the CarMaker suspension

response is represented through the suspension measurement covariance in the Kalman filter.

Combining the suspension components, the final suspension-based wheel-load estimate at wheel i and discrete time sample k is

$$F_{z,i,k}^{\text{total}} = F_{z,i,0} + F_{z,i}^{\text{spr}}(d_{i,k}) + F_{z,i}^{\text{dam}}(v_{i,k}) + F_{z,i}^{\text{arb}}(\Delta\eta_{a(i),k}), \tag{9}$$

where $d_{i,k}$ and $v_{i,k}$ denote the suspension compression and compression velocity of wheel i at sample k, respectively. The term $a(i)$ denotes the axle associated with wheel i, and $\Delta\eta_{a(i),k}$ is the corresponding differential ARB deformation input for that axle. The static offset $F_{z,i,0}$ is initialized from the static wheel-load distribution or from the first sample under a nominal operating condition.

The resulting suspension-based wheel-load estimate is used as a pseudo-measurement in the Kalman filtering framework described in Section III. In real suspensions, motion-ratio variation, linkage geometry, bump-stop engagement, and nonlinear damper characteristics can produce deviations from the simplified component models, especially over large travel ranges. The present study therefore uses low-order spring, damper, and ARB representations to capture the dominant force trends while maintaining a compact estimator structure. The remaining model mismatch is accounted for through the suspension measurement covariance in the Kalman filtering formulation described in Section III. The spring, damper, and anti-roll-bar force models are illustrated in Fig. 2, together with representative CarMaker-derived force samples.

C. Design rationale

The suspension model is modular with respect to the Kalman filtering framework. Changes to the suspension model affect only the wheel-load pseudo-measurements supplied to the filter, while the state definition, measurement structure, and update equations remain unchanged. The component model is also modular internally, since the spring, damper, and anti-roll-bar effects are constructed as separate additive terms that can be refined independently.

In the present implementation, a linear spring law, a piecewise-linear damper model, and a linear anti-roll-bar term are used to capture the dominant suspension effects with minimal complexity. Among these, the anti-roll bar is particularly important for representing axle-level load coupling, while the asymmetric damper model provides a secondary refinement of the model fidelity. If needed, the model can be extended with a full damper map, nonlinear spring behavior, bump-stop terms, or more detailed motion-ratio formulations without changing the Kalman filter state definition or update equations.

III. Physics-Constrained Kalman Filtering Framework

A. Estimator overview

The objective of the estimator is to reconstruct the four individual wheel normal loads,

$$\boldsymbol{x}_k = \begin{bmatrix} F_{z,\text{FL},k} & F_{z,\text{FR},k} & F_{z,\text{RL},k} & F_{z,\text{RR},k} \end{bmatrix}^\top. \tag{10}$$

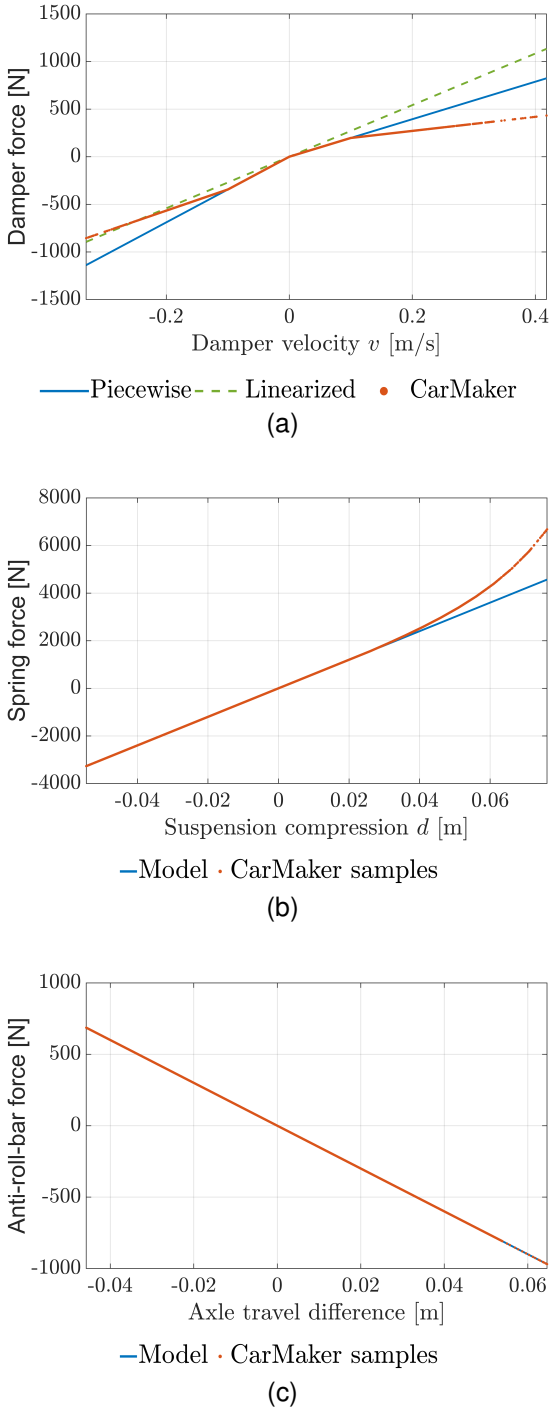

Fig. 2. Proposed suspension models compared with CarMaker-simulated force data: (a) damper force, (b) spring force, and (c) anti-roll-bar force.

The proposed framework combines two complementary sources of information. The first is the suspension-based wheel-load estimate developed in Section II-B, which provides local wheel-resolved force information. The second is the set of IMU-based rigid-body equilibrium relations, which provides global vehicle-level force and moment consistency.

These two sources are fused through a sequential two-stage Kalman filtering framework. The suspension-based pseudo-measurements are first used to update the wheel-load states, and the IMU-based equilibrium relations are then imposed as

soft probabilistic physical constraints. This structure allows the estimator to retain local sensitivity to suspension-induced load variations while enforcing global physical consistency in the wheel-load distribution.

B. Reference frame and IMU convention

All quantities entering the rigid-body equilibrium relations are expressed in the IMU-aligned body frame $\{\mathcal{B}\}$ to avoid explicit attitude estimation. The axes $(x_{\mathcal{B}}, y_{\mathcal{B}}, z_{\mathcal{B}})$ are aligned with the IMU, with $x_{\mathcal{B}}$ forward, $y_{\mathcal{B}}$ left, and $z_{\mathcal{B}}$ upward.

The accelerometer outputs $(a_{x,k}, a_{y,k}, a_{z,k})$ are interpreted as specific force resolved in $\{\mathcal{B}\}$, meaning that gravity is included. Consequently, for a stationary vehicle on level ground,

$$a_{z,k} \approx g. \tag{11}$$

This convention allows the vertical force balance to be expressed directly using $a_{z,k}$, without reconstructing gravity through explicit attitude estimation. The formulation assumes negligible IMU misalignment or prior alignment compensation.

C. Process and measurement models

The wheel-load state is modeled as a random-walk process,

$$\boldsymbol{x}_k = \boldsymbol{x}_{k-1} + \boldsymbol{w}_{k-1}, \qquad \boldsymbol{w}_{k-1} \sim \mathcal{N}(\mathbf{0}, \mathbf{Q}), \tag{12}$$

where $\boldsymbol{w}_{k-1}$ is the process-noise vector and $\mathbf{Q} \in \mathbb{R}^{4\times4}$ is the process-noise covariance matrix. A random-walk model is adopted because the wheel normal loads vary with road excitation, suspension motion, inertial load transfer, and other effects that are difficult to describe with a compact deterministic process model [32], [33].

The suspension-based wheel-load estimate developed in Section II-B is used as a pseudo-measurement of the wheel-load state:

$$\begin{aligned}\boldsymbol{z}_k^{\mathrm{susp}} &= \begin{bmatrix} F_{z,\mathrm{FL},k}^{\mathrm{total}} & F_{z,\mathrm{FR},k}^{\mathrm{total}} & F_{z,\mathrm{RL},k}^{\mathrm{total}} & F_{z,\mathrm{RR},k}^{\mathrm{total}} \end{bmatrix}^\top \\ &= \boldsymbol{x}_k + \boldsymbol{v}_{s,k}, \qquad \boldsymbol{v}_{s,k} \sim \mathcal{N}(\mathbf{0}, \mathbf{R}_s),\end{aligned} \tag{13}$$

where $\boldsymbol{z}_k^{\mathrm{susp}}$ denotes the vector of suspension-based wheel-load pseudo-measurements and $\mathbf{R}_s$ is the corresponding covariance. The covariance $\mathbf{R}_s$ represents the uncertainty of the suspension-based pseudo-measurements, including sensor noise and residual mismatch in the suspension-based wheel-load model.

In addition to the local suspension-based pseudo-measurements, the estimated wheel loads are required to satisfy vehicle-level rigid-body equilibrium. Following standard vehicle-dynamics load-transfer formulations [34], [35], the vertical-force, pitch-moment, and roll-moment equilibrium relations can be written compactly as

$$\mathbf{A}\boldsymbol{x}_k = \boldsymbol{b}_k, \tag{14}$$

where $\mathbf{A}$ is the rigid-body relation matrix and $\boldsymbol{b}_k$ is the corresponding equilibrium vector constructed from IMU signals and aerodynamic loading.

The rigid-body relation matrix is

$$\mathbf{A} = \begin{bmatrix} 1 & 1 & 1 & 1 \\ l_f & l_f & -l_r & -l_r \\ -\frac{T_f}{2} & \frac{T_f}{2} & -\frac{T_r}{2} & \frac{T_r}{2} \end{bmatrix}, \tag{15}$$

where l_f and l_r are the longitudinal distances from the center of gravity to the front and rear axles, respectively, and T_f and T_r are the front and rear track widths. The corresponding equilibrium vector is

$$\boldsymbol{b}_k = \begin{bmatrix} ma_{z,k} - F_{z,\mathrm{aero},k} \\ mh_{cg}a_{x,k} + (x_{\mathrm{aero}} - x_{cg})F_{z,\mathrm{aero},k} \\ mh_{cg}a_{y,k} \end{bmatrix}, \tag{16}$$

where m is the vehicle mass, h_{cg} is the center-of-gravity height, and x_{cg} and x_{aero} denote the longitudinal positions of the center of gravity and aerodynamic center of pressure, respectively, in the same vehicle-fixed coordinate frame.

Rather than enforcing (14) as an exact equality, the equilibrium relation is introduced as a soft probabilistic physical constraint:

$$\boldsymbol{b}_k = \mathbf{A}\boldsymbol{x}_k + \boldsymbol{w}_{c,k}, \qquad \boldsymbol{w}_{c,k} \sim \mathcal{N}(\mathbf{0}, \mathbf{R}_c), \tag{17}$$

where $\boldsymbol{w}_{c,k}$ represents the constraint uncertainty and $\mathbf{R}_c$ determines the strength of constraint enforcement. This formulation follows the principle of constrained Kalman filtering, in which physical equality relations are incorporated into recursive state estimation while allowing uncertainty in the constraint equations [25], [27], [28].

The aerodynamic vertical force is modeled as

$$F_{z,\mathrm{aero},k} = \frac{1}{2}\rho V_{x,k}^2 A_{\mathrm{ref}} c_{L0}, \tag{18}$$

where ρ is the air density, $V_{x,k}$ is the longitudinal vehicle speed, A_{ref} is the aerodynamic reference area, and c_{L0} is the zero-yaw vertical aerodynamic coefficient. Here, $F_{z,\mathrm{aero},k}$ follows the sign convention of (16): positive values correspond to aerodynamic lift and reduce the tire normal-load sum, whereas negative values correspond to aerodynamic downforce. Including this term reduces speed-dependent bias in both the total normal load and its front–rear distribution [34], [36].

D. Two-stage Kalman update

At each time step, the estimator performs one prediction step followed by two sequential measurement updates. The first update uses the suspension-based pseudo-measurements, and the second update applies the IMU-based rigid-body equilibrium relations as soft physical constraints.

1) Prediction: From the random-walk process model in (12), the prediction step is

$$\boldsymbol{x}_{k|k-1} = \boldsymbol{x}_{k-1|k-1}, \qquad \mathbf{P}_{k|k-1} = \mathbf{P}_{k-1|k-1} + \mathbf{Q}, \tag{19}$$

where $\mathbf{P}_{k|k-1}$ is the predicted state-error covariance and $\mathbf{P}_{k-1|k-1}$ is the posterior covariance from the previous time step. The covariance $\mathbf{Q}$ controls the responsiveness of the estimator to wheel-load variations not captured by the random-walk prediction alone.

2) Suspension-based update: Based on the suspension pseudo-measurement model in (13), the suspension-update gain is

$$\mathbf{K}_s = \mathbf{P}_{k|k-1}\left(\mathbf{P}_{k|k-1} + \mathbf{R}_s\right)^{-1}. \tag{20}$$

The intermediate posterior state estimate is then obtained as

$$\boldsymbol{x}_k^{(s)} = \boldsymbol{x}_{k|k-1} + \mathbf{K}_s\left(\boldsymbol{z}_k^{\mathrm{susp}} - \boldsymbol{x}_{k|k-1}\right), \tag{21}$$

and the corresponding covariance update is

$$\mathbf{P}_k^{(s)} = \left(\mathbf{I}_4 - \mathbf{K}_s\right)\mathbf{P}_{k|k-1}\left(\mathbf{I}_4 - \mathbf{K}_s\right)^\top + \mathbf{K}_s\mathbf{R}_s\mathbf{K}_s^\top. \tag{22}$$

This first update injects local wheel-resolved force information into the estimator.

3) Physics-constraint update: Using the suspension-updated estimate as the prior, the rigid-body equilibrium relations are applied through the soft constraint model in (17). The constraint-update gain is

$$\mathbf{K}_c = \mathbf{P}_k^{(s)}\mathbf{A}^\top\left(\mathbf{A}\mathbf{P}_k^{(s)}\mathbf{A}^\top + \mathbf{R}_c\right)^{-1}, \tag{23}$$

and the final posterior state estimate is

$$\boldsymbol{x}_{k|k} = \boldsymbol{x}_k^{(s)} + \mathbf{K}_c\left(\boldsymbol{b}_k - \mathbf{A}\boldsymbol{x}_k^{(s)}\right). \tag{24}$$

The covariance update is

$$\mathbf{P}_{k|k} = \left(\mathbf{I}_4 - \mathbf{K}_c\mathbf{A}\right)\mathbf{P}_k^{(s)}\left(\mathbf{I}_4 - \mathbf{K}_c\mathbf{A}\right)^\top + \mathbf{K}_c\mathbf{R}_c\mathbf{K}_c^\top. \tag{25}$$

This second update regularizes the wheel-load estimates by enforcing global vehicle-level force and moment consistency.

E. Measurement structure and interpretation

The suspension pseudo-measurement model in (13) provides one direct pseudo-measurement for each wheel normal load. Therefore, the suspension update supplies wheel-resolved information for all four states. In contrast, the rigid-body constraint model in (17) provides three vehicle-level consistency relations: vertical-force, pitch-moment, and roll-moment equilibrium.

The constraint matrix $\mathbf{A} \in \mathbb{R}^{3\times4}$ has rank three under normal vehicle geometry. Thus, the rigid-body equilibrium relations alone cannot uniquely determine the four wheel normal loads. Instead, they provide three independent physical consistency conditions that couple the corner loads through global vehicle dynamics.

Consequently, the primary role of the constraint update is not to recover the wheel normal loads by itself, but to regularize the suspension-based local estimates by enforcing physically consistent load redistribution across the vehicle. This interpretation is central to the proposed framework: the suspension update provides local wheel-level sensitivity, while the constraint update provides global physical consistency.

F. Implementation details

The estimator is implemented as a sequential two-stage Kalman filter. The per-sample estimation cycle is summarized in Fig. 3. First, a random-walk prediction is performed. Second, wheel-level suspension pseudo-measurements are used to update the load estimates. Third, IMU-based soft rigid-body equilibrium constraints, including the aerodynamic correction, are applied as a second measurement update.

This modular structure separates pseudo-measurement construction from the Kalman filter core, allowing the suspension model to be refined without changing the state definition or the constraint-update structure.

G. Computational considerations

The estimator employs a fixed four-state Kalman filter, so the per-sample computational cost remains constant for the implemented formulation. In a generic Kalman filter, the update step scales as $\mathcal{O}(n^3)$, where n is the state dimension, because of matrix inversion and dense linear-algebra operations [32], [33], [37]. For the present estimator, $n = 4$, so the computation reduces to fixed-size matrix operations.

In the proposed two-stage update, the dominant cost is the solution of one 4×4 and one 3×3 dense linear system, corresponding to approximately 1–2 kFLOPs per sample, or about 0.1–0.2 MFLOPs/s at 100 Hz. These requirements are modest relative to the capabilities of modern automotive microcontrollers with hardware floating-point support. For reference, Infineon AURIX TC4xx devices provide 32-bit floating-point units in all CPUs, with a published throughput of 2 FLOPs per cycle at real-time core frequencies up to 500 MHz [38]. This comparison indicates that the proposed estimator is computationally lightweight, although the present work does not include processor-level runtime benchmarking or implementation profiling on production hardware.

IV. Simulation Validation

A. Simulation environment and test vehicle

All estimator validation was performed in IPG CarMaker 15 (CarMaker for Simulink 15.0) using the built-in *typical sports car* dataset with a 4WD driveline and an Audi R8 2016 visual model shown in Fig. 4. The simulation platform provides a controlled environment in which individual wheel normal loads, suspension states, and body motions are available simultaneously, enabling direct benchmarking of the estimator output against the CarMaker reference signals.

Key geometric, inertial, aerodynamic, and suspension parameters extracted from the vehicle information file are summarized in Table I. These parameters were used both to configure the proposed estimator and to define the baseline methods in a consistent manner, ensuring a fair comparison across all approaches.

B. Evaluation setup, compared methods, and metrics

The validation is structured to assess the proposed estimator from complementary perspectives. The ISO double lane change evaluates transient performance under strong

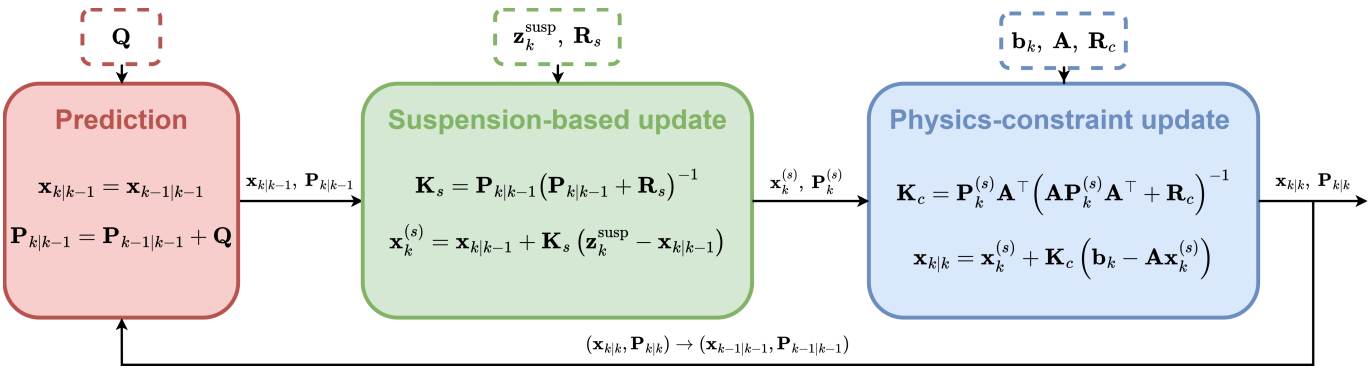

Fig. 3. Block-diagram representation of the proposed wheel-load estimator. Suspension measurements are first converted into wheel-level pseudo-measurements, which are fused through a prediction step and a suspension update. IMU-based vertical-force, pitch-moment, and roll-moment equilibrium relations are then applied as soft constraints in a second update stage.

TABLE I
PRIMARY CARMAKER VEHICLE PARAMETERS USED IN SIMULATION VALIDATION.

Parameter	Symbol	Value
Sprung mass (rigid body)	m	1424.2 kg
CG / body reference location	(x_{cg}, y_{cg}, z_{cg})	(2.267, 0, 0.497) m
Body inertia about reference	(I_{xx}, I_{yy}, I_{zz})	(518.04, 1677.0, 1921.3) kg m^2
Wheelbase	L	2.8 m
CG distances to axles	(l_f, l_r)	(1.223, 1.527) m
Track widths	(T_f, T_r)	(1.632, 1.582) m
Tires	–	Front 245/35 R19; rear 295/35 R19
Aerodynamic reference area	A_{ref}	2.1 m^2
Aerodynamic application point	(x_{aero}, y, z)	(2.08, 0, 0.62) m
Nominal lift coefficient	c_{L0}	0.149 at 0° yaw
Front spring rate	k_f	60 000.0 N/m
Rear spring rate	k_r	70 000.0 N/m
Anti-roll bar stiffness	$(k_{\text{arb},f}, k_{\text{arb},r})$	15 000.0 N/m front and rear, Hookean
Front damper map	–	Push: (0.1 m/s, 196.9 N), (1.0 m/s, 861.97 N); pull: (0.1 m/s, 344.69 N), (1.0 m/s, 2339.9 N)
Rear damper map	–	Push: (0.1 m/s, 198.66 N), (1.0 m/s, 879.62 N); pull: (0.1 m/s, 312.15 N), (1.0 m/s, 2014.6 N)
Bump-stop engagement	$(d_{0,f}, d_{0,r})$	(0.026, 0.040) m, buffer `tz0`
IMU sensor location	(x, y, z)	(2.107, 0, 0.497) m

Fig. 4. CarMaker test vehicle used for estimator validation (Audi R8 2016).

suspension excitation, while the Nürburgring and Hockenheim full-lap scenarios assess robustness under sustained combined maneuvers and elevation changes. Together, these experiments examine whether the estimator can retain local sensitivity to suspension-induced load variations while maintaining global physical consistency in the wheel-load distribution.

All estimators were evaluated on identical CarMaker simulation logs using the four wheel normal loads $\{F_{z,\text{FL}}, F_{z,\text{FR}}, F_{z,\text{RL}}, F_{z,\text{RR}}\}$ as reference. To ensure fairness, all baseline methods were implemented using the same vehicle parameters and sensor signals. Where necessary, parameters were tuned within physically reasonable ranges to provide each method with comparable operating conditions.

The following methods were compared:

- **Method A**: the **proposed** physics-constrained Kalman filter, combining suspension-based wheel-load pseudo-measurements with IMU-based rigid-body equilibrium constraints;
- **Method B**: an algebraic normal-load estimator based on the formulation of Alatorre et al. [15], in which road grade and bank are approximated from low-frequency suspension-derived pitch and roll;
- **Method C**: a rigid-body quasi-static (QS) load-transfer baseline anchored to static axle loads;
- **Method D**: a suspension-only baseline corresponding to the proposed suspension-based wheel-load model evaluated without Kalman filtering or explicit constraint enforcement;

- **Method E**: a quarter-car vertical tire-force observer based on Cheon et al. [12], adapted to the available full-car CarMaker signals by reconstructing per-corner inputs from the body IMU and suspension measurements;
- **Method F**: a per-corner vertical tire-force estimator based on Ding et al. [1], implemented as a strong-tracking unscented Kalman filter (STUKF) using suspension compression and compression-rate measurements, and adapted to the available CarMaker suspension signals.

These methods were selected to test the proposed estimator against complementary baseline classes that reflect the main trade-offs in wheel normal load estimation. Method B represents a rigid-body-equilibrium-based estimator and was included because this class directly addresses vehicle-level force and moment balance. Method C provides a quasi-static load-transfer baseline, which remains a standard reference in many practical vehicle-dynamics frameworks due to its simplicity and low computational cost. Method D represents a suspension-only formulation and was included to isolate the contribution of the suspension-based wheel-load model independently of Kalman filtering and explicit constraint enforcement. Methods E and F were selected as recent literature-based observer formulations. Method E corresponds to a reduced-order suspension-based observer, whereas Method F represents a stochastic filtering approach based on suspension measurements. Collectively, these baselines span rigid-body, quasi-static, suspension-only, reduced-order observer-based, and stochastic filtering approaches, thereby providing a diverse comparison across methods that emphasize local suspension information, global load-transfer relations, or observer-based fusion.

Validation is presented in two stages of increasing complexity. First, an ISO double lane change is used as a standardized transient-handling maneuver with pronounced lateral load transfer. Second, full-lap results on the Nürburgring and Hockenheim circuits evaluate estimator performance under sustained combined excitation, elevation change, and track-dependent maneuver severity.

Let the wheel-load estimation error for wheel $i \in \{\mathrm{FL}, \mathrm{FR}, \mathrm{RL}, \mathrm{RR}\}$ be defined as

$$e_i(t_k) = \hat{F}_{z,i}(t_k) - F_{z,i}^{\mathrm{ref}}(t_k). \tag{26}$$

Performance is primarily reported using per-wheel error metrics over a common evaluation window. For each wheel, the root-mean-square error (RMSE), 95th-percentile absolute error, and maximum absolute error are defined as

$$\mathrm{RMSE}_i = \sqrt{\frac{1}{N}\sum_{k=1}^{N} e_i^2(t_k)}, \tag{27}$$

$$P95_i = \mathrm{percentile}_{95}\left(|e_i(t_k)|\right), \tag{28}$$

$$\mathrm{Max}_i = \max_k |e_i(t_k)|, \tag{29}$$

where N is the number of samples in the evaluation window.

In addition, a normalized root-mean-square error is reported as

$$\mathrm{RMSE}_{\%,i} = 100 \times \frac{\mathrm{RMSE}_i}{\overline{F_{z,i}^{\mathrm{ref}}}}, \tag{30}$$

where $\overline{F_{z,i}^{\mathrm{ref}}}$ denotes the mean reference wheel normal load for wheel i over the same evaluation window.

For the ablation and Monte Carlo studies, aggregate metrics are also reported by pooling errors across all four wheels and all samples. These pooled metrics are used to summarize overall estimator robustness without emphasizing wheel-specific effects. The aggregate RMSE, 95th-percentile absolute error, and maximum absolute error are defined as

$$\mathrm{RMSE}_{\mathrm{agg}} = \sqrt{\frac{1}{4N}\sum_{i=1}^{4}\sum_{k=1}^{N} e_i^2(t_k)}, \tag{31}$$

$$P95_{\mathrm{agg}} = \mathrm{percentile}_{95}\Big(\{|e_i(t_k)|\}_{i=1,\ldots,4;\, k=1,\ldots,N}\Big), \tag{32}$$

$$\mathrm{Max}_{\mathrm{agg}} = \max_{i,k} |e_i(t_k)|. \tag{33}$$

When reported, the aggregate percentage RMSE is defined as

$$\mathrm{RMSE}_{\%,\mathrm{agg}} = 100 \times \frac{\mathrm{RMSE}_{\mathrm{agg}}}{\frac{1}{4}\sum_{i=1}^{4}\overline{F_{z,i}^{\mathrm{ref}}}}. \tag{34}$$

For the Monte Carlo noise study, these aggregate metrics are evaluated for each trial and then summarized across trials using the sample mean μ and sample standard deviation σ.

C. ISO double lane change evaluation

Table II summarizes the wheel-load estimation errors over the trimmed maneuver interval ($5.0\,\mathrm{s}$ to $12.0\,\mathrm{s}$), with corresponding time-history comparisons and error summaries shown in Figs. 5 and 6, respectively. In this scenario, Methods D and F provide the lowest errors overall. Method D achieves the lowest RMSE on the FL and RL wheels, whereas Method F achieves the lowest RMSE on the FR and RR wheels. The same trend is observed in the normalized RMSE values, with Method D performing best on the left-side wheels and Method F on the right-side wheels.

Among the remaining methods, the proposed physics-constrained Kalman filter (Method A) provides the strongest overall performance. It consistently outperforms the algebraic baseline (Method B), the quasi-static load-transfer model (Method C), and the reduced-order observer (Method E), while maintaining similar error levels across all four wheels. This indicates that the proposed framework remains well balanced across the vehicle under a highly transient maneuver, even though it does not achieve the minimum error on any individual corner in this test.

The ISO double lane change is characterized by rapid lateral load transfer and strong transient suspension excitation. Under these conditions, the suspension-dominant formulations of Methods D and F appear particularly well matched to the short-duration wheel-load redistribution. By contrast, Method E yields the largest errors, while Method C also remains clearly less accurate than Methods A, D, and F, indicating that simpler or more weakly coupled formulations are less effective in reproducing the fast load variations induced by this maneuver.

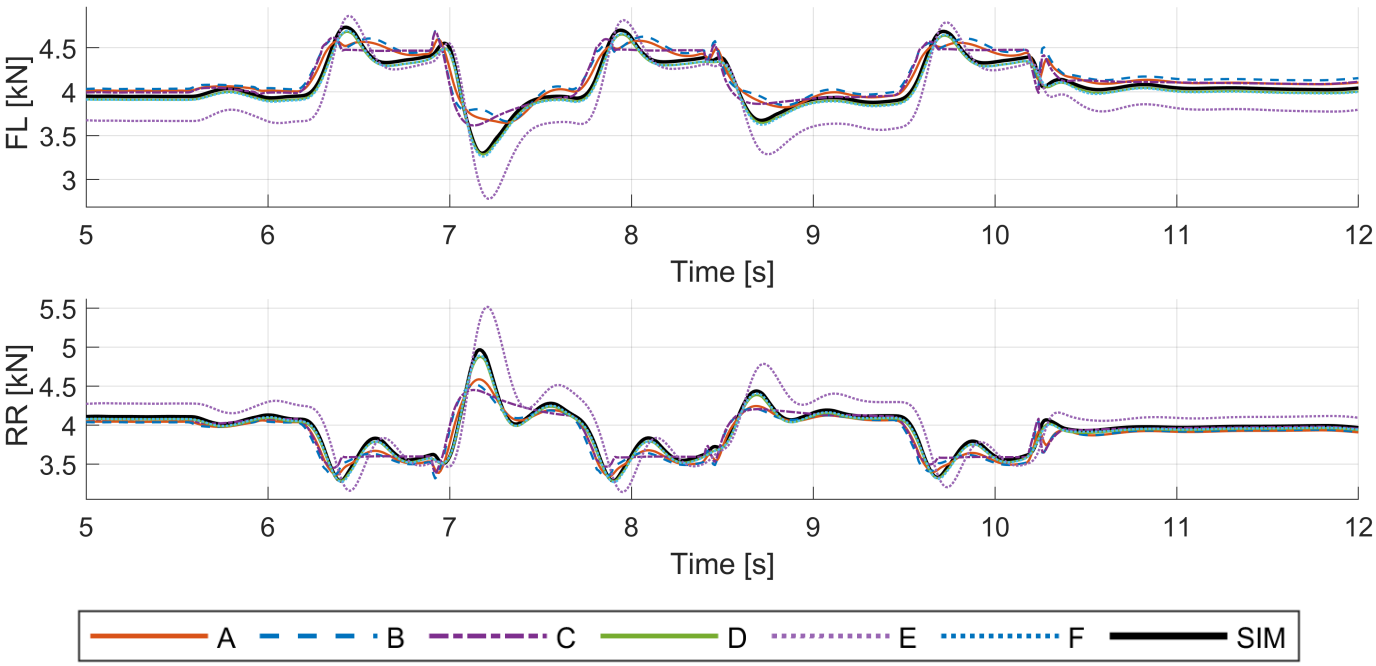

Fig. 5. Estimated and reference wheel normal loads during the trimmed ISO double lane change maneuver.

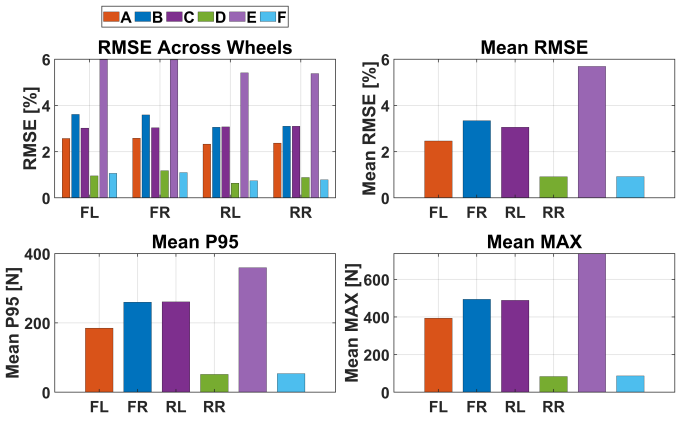

Fig. 6. Wheel-load estimation error metric bar chart over the ISO double lane change scenario.

Overall, the ISO double lane change serves as an isolated transient benchmark. The results show that while Methods D and F provide the lowest maneuver-specific errors, Method A maintains competitive accuracy together with physically consistent load distribution across all four wheels.

D. Full-lap evaluation

Following the controlled ISO DLC, estimator performance is evaluated over complete laps of the Nürburgring and Hockenheim circuits. These scenarios provide a comprehensive validation environment, combining sustained longitudinal and lateral excitation with elevation changes. Representative track sections used in the evaluation are shown in Fig. 7.

The Nürburgring represents the more demanding case due to its significant elevation variation and frequent combined maneuvers, as illustrated by the selected segments in Fig. 7(a)–(c), whereas Hockenheim offers a smoother and more uniform excitation profile (Fig. 7(d)).

TABLE II
WHEEL-LOAD ESTIMATION ERROR METRICS OVER THE ISO DOUBLE LANE CHANGE SCENARIO. METHODS A-F CORRESPOND TO THE ESTIMATORS REPORTED IN THE EVALUATION RESULTS.

Metric	Method	FL	FR	RL	RR
RMSE [N]	A	83.58	84.47	78.07	77.92
	B	124.39	124.82	87.77	87.37
	C	155.65	155.70	169.47	169.67
	D	**38.89**	48.08	**25.08**	34.73
	E	244.99	244.73	212.92	211.92
	F	43.36	**44.87**	29.04	**30.80**
RMSE [%]	A	1.96	1.98	2.08	2.08
	B	2.91	2.92	2.34	2.33
	C	3.64	3.65	4.52	4.52
	D	**0.95**	1.17	**0.64**	0.88
	E	5.98	5.97	5.41	5.38
	F	1.06	**1.09**	0.74	**0.78**
P95 [N]	A	161.76	157.08	124.09	122.36
	B	180.53	176.53	140.11	147.99
	C	380.77	361.36	481.45	485.77
	D	**56.75**	**65.38**	**35.76**	**47.02**
	E	377.49	376.72	340.68	341.43
	F	60.81	65.12	40.50	48.29
MAX [N]	A	394.62	407.88	392.36	379.75
	B	496.41	515.44	494.64	470.32
	C	467.73	400.98	555.97	530.16
	D	74.79	**80.43**	**84.65**	**93.99**
	E	615.56	615.76	860.49	857.74
	F	**71.73**	80.79	88.73	106.59

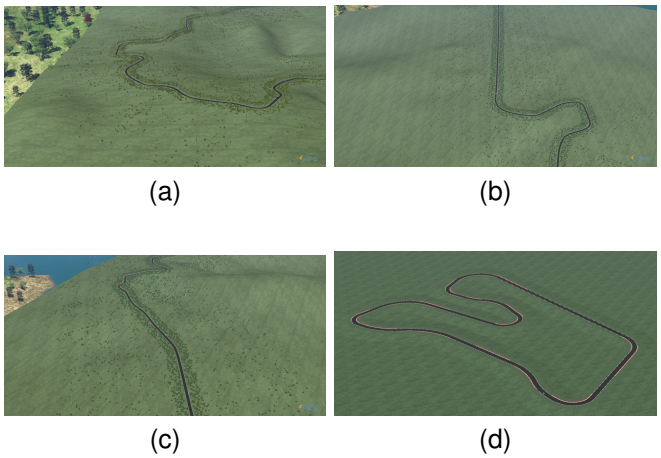

Fig. 7. Representative images of the evaluated track sections. (a) Segment 09: Karussell. (b) Segment 11: Kleine Karussell. (c) Segment 12: Antoniusbuche. (d) Hockenheim circuit.

Tables III and IV summarize the full-lap error statistics, with corresponding visual summaries provided in Figs. 9 and 10.

On the Nürburgring, the proposed physics-constrained Kalman filter (Method A) achieves the best overall performance, with RMSE values between 158 and 243 N across the four wheels and a 76–85% reduction compared with the quasi-static baseline (Method C), as also illustrated in Fig. 9. Method A consistently yields the lowest errors among the compared methods. Despite its strong performance in the ISO double lane change test, Method F yields the largest errors after the quasi-static baseline in the full-lap evaluation, suggesting that strong performance in an isolated transient maneuver does not necessarily translate to reliable full-lap wheel normal load estimation.

On the Hockenheim circuit, all methods exhibit reduced errors owing to the less severe excitation. Method A again delivers the best accuracy, with RMSE values between 77 and 98 N (approximately 2%), demonstrating robust performance across varying operating conditions, as reflected in Fig. 10. Method B remains the next strongest baseline, whereas Methods D and E show intermediate performance. Method F produces substantially larger errors than Methods A and B across all wheels on Hockenheim and does not improve upon the simpler algebraic formulation in this scenario.

Figure 8 illustrates representative front-left wheel normal-load histories for both circuits. The quasi-static method deviates substantially from the reference during combined maneuvers, whereas Method A closely tracks the simulated loads. Method B captures the general trend but exhibits larger transient deviations, and Method E remains limited by its independent quarter-car structure.

Overall, the full-lap results confirm that while suspension-only approaches (Method D) can perform well when excitation is dominated by local suspension dynamics, the proposed physics-constrained framework provides superior robustness and accuracy under realistic driving conditions involving global load redistribution.

TABLE III
WHEEL-LOAD ESTIMATION ERROR METRICS OVER THE NÜRBURGRING SCENARIO.

Metric	Method	FL	FR	RL	RR
RMSE [N]	A	**231.68**	**212.73**	**243.11**	**158.07**
	B	467.78	274.92	375.75	226.36
	C	998.56	1010.40	1017.10	1032.50
	D	582.57	610.56	456.55	418.64
	E	729.12	682.65	453.89	440.88
	F	888.40	903.71	752.45	713.00
RMSE [%]	A	**5.18**	**5.01**	**6.19**	**4.27**
	B	10.46	6.47	9.56	6.11
	C	22.34	23.78	25.89	27.89
	D	13.03	14.37	11.62	11.31
	E	16.31	16.07	11.55	11.91
	F	19.87	21.27	19.15	19.26
P95 [N]	A	**406.43**	**418.68**	**405.23**	**306.13**
	B	827.06	551.54	690.29	447.70
	C	1911.50	1972.40	1891.50	1940.40
	D	1102.30	1222.40	899.69	855.96
	E	1307.60	1310.90	895.85	880.41
	F	1593.50	1714.70	1412.10	1270.80
MAX [N]	A	**1739.30**	**1586.00**	**1509.60**	**1778.80**
	B	2020.70	1938.50	1917.20	1579.30
	C	4695.00	5932.10	4832.40	5415.70
	D	2871.20	3724.10	2170.40	2291.40
	E	2155.90	2305.40	2551.20	2111.30
	F	2716.50	3989.10	2006.10	2143.30

E. Ablations

1) Ablation analysis of estimator components: To quantify the influence of individual model and estimator components, an ablation study was conducted using the Nürburgring scenario, which provides the most demanding combination of longitudinal, lateral, and elevation excitations. The results are presented in Table V.

Removing the aerodynamic vertical force term from the vertical equilibrium constraint increased the aggregate RMSE from 213.9 N to 236.8 N (+10.7%) and the $P95$ error from 393.6 N to 492.9 N (+25.2%), confirming that explicit aerodynamic compensation mitigates a speed-dependent bias in the total-load constraint.

Eliminating the rigid-body equilibrium constraints caused a marked degradation in performance, increasing the aggregate RMSE from 213.9 N to 521.9 N (+144.0%) and the $P95$ error from 393.6 N to 1051.9 N (+167.3%). This demonstrates that the second-stage physics-constraint update is essential for enforcing global physical consistency across the vehicle. Disabling the ARB contribution increased the RMSE from 213.9 N to 283.8 N (+32.7%), indicating that roll-coupling forces play a significant role in capturing lateral load redistribution. A constraint-strength sweep further revealed an optimum at the nominal setting (R_c scale $= 1$), with both overly tight and overly weak constraints leading to reduced accuracy.

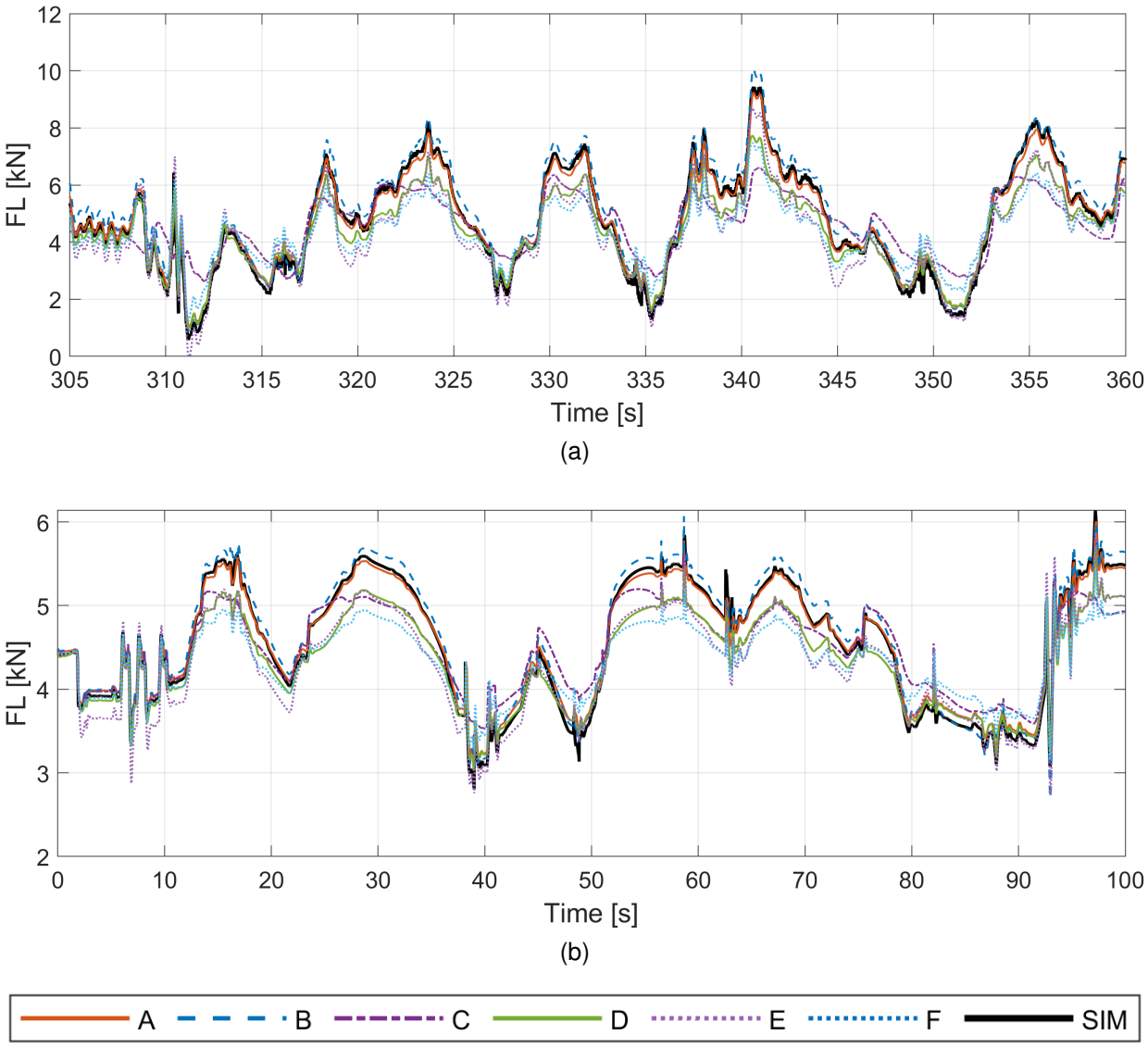

Fig. 8. Comparison of wheel normal-load estimation methods for the selected driving cases. (a) Karussell segment from the Nürburgring simulation case. (b) Single lap from the Hockenheim simulation case.

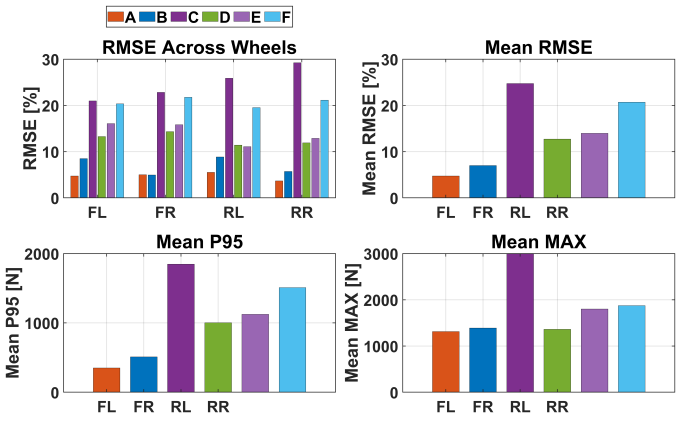

Fig. 9. Wheel-load estimation error metric bar chart Nürburgring scenario.

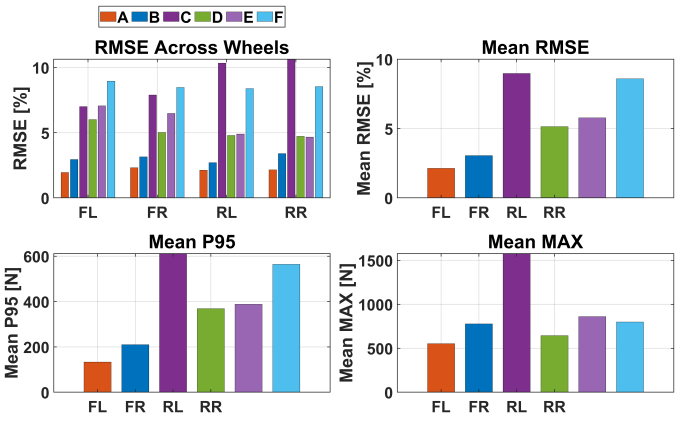

Fig. 10. Wheel-load estimation error metric bar chart Hockenheim scenario.

In contrast, replacing the asymmetric push/pull damper model with a symmetric linear damper produced negligible changes in the aggregate error metrics (Table V). This suggests that, for the evaluated driving conditions, the estimator perfor-

TABLE IV
WHEEL-LOAD ESTIMATION ERROR METRICS OVER THE HOCKENHEIM SCENARIO.

Metric	Method	FL	FR	RL	RR
RMSE [N]	A	**87.36**	**97.50**	**83.74**	**76.61**
	B	143.41	134.34	101.18	120.31
	C	323.75	331.01	415.50	378.53
	D	289.64	209.07	194.48	173.27
	E	335.89	264.56	187.01	163.20
	F	426.11	353.98	336.03	309.21
RMSE [%]	A	**1.90**	**2.34**	**2.15**	**2.21**
	B	3.11	3.22	2.60	3.47
	C	7.03	7.93	10.66	10.92
	D	6.29	5.01	4.99	5.00
	E	7.29	6.34	4.80	4.71
	F	9.25	8.48	8.62	8.92
P95 [N]	A	**150.31**	**142.06**	**115.15**	**116.85**
	B	225.50	222.17	195.02	190.41
	C	551.65	517.30	653.94	690.53
	D	468.53	393.19	304.39	334.33
	E	483.96	473.77	312.35	259.24
	F	638.24	590.34	524.42	485.57
MAX [N]	A	**539.13**	**450.23**	686.14	**550.24**
	B	559.29	990.41	947.33	723.62
	C	1279.50	1930.40	1833.50	1267.30
	D	1045.10	972.51	791.41	897.16
	E	1027.00	915.20	759.03	739.41
	F	926.32	850.21	**655.97**	779.60

mance is dominated by the suspension spring information and the global physics-constraint update, while damper asymmetry provides limited measurable benefit.

2) Structural comparison using the Cheon observer: To isolate the contribution of the global constraint update, an additional comparison was performed using the quarter-car vertical tire-force observer of [12] adapted to the available full-car CarMaker signals. Two variants were considered: (i) *Cheon-independent*, in which the four corner observers operate independently, and (ii) *Cheon + Constraint Kalman Filter*, where the per-corner Cheon outputs are refined using the proposed IMU-based soft equilibrium update. The latter is not treated as an external baseline but rather as a structural fairness study.

On the Nürburgring benchmark, the independent Cheon implementation yielded an aggregate RMSE of 591.2 N, $P95$ of 1204.9 N, and a maximum error of 2551.2 N. Incorporating the same global constraint update reduced these metrics to RMSE 325.6 N, $P95$ 658.1 N, and maximum error 1646.6 N, corresponding to reductions of 44.9%, 45.4%, and 35.5%, respectively. These results demonstrate that a substantial portion of the performance improvement arises from enforcing global vertical-force and pitch/roll moment consistency across the four wheels.

Despite this improvement, the Cheon-based front end with the constraint update remains less accurate than the proposed suspension-based front end with the same physics-constrained filtering structure. This comparison supports the interpretation that the global constraint update is the primary source of robustness, while the proposed suspension-based pseudo-measurements provide additional accuracy gains.

TABLE V
ABLATION STUDY: AGGREGATE WHEEL-LOAD ERROR METRICS POOLED ACROSS ALL FOUR WHEELS (NÜRBURGRING SCENARIO).

Case	RMSE [N]	RMSE [%]	P95 [N]	Max [N]
Baseline (all ON)	**213.9**	**5.23**	**393.6**	1778.8
No Aero	236.8	5.79	492.9	1757.7
No ARB	283.8	6.94	522.7	1765.9
Symmetric Damper	214.4	5.24	394.5	1769.4
No Constraints	521.9	12.77	1051.9	3365.9
R_c scale $= 0.25$	235.1	5.75	452.1	1975.7
R_c scale $= 0.5$	222.3	5.44	421.2	1924.4
R_c scale $= 2$	296.1	7.24	565.0	**1621.8**
R_c scale $= 4$	411.1	10.06	802.5	2367.6

F. Monte Carlo noise scaling study

A Monte Carlo noise-scaling study was performed to assess the sensitivity of the proposed physics-constrained Kalman filter to accelerometer and suspension-displacement uncertainty. Starting from a fixed CarMaker log, synthetic noise was injected into the measured accelerometer channels and suspension displacement signals before estimator pre-filtering and numerical differentiation, so that the perturbations propagated into the derived suspension velocities and wheel-load estimates. To perturb the full suspension pseudo-measurement path consistently, the same displacement-sensor error realization was also applied to the wheel-travel channels used by the anti-roll-bar term.

Noise models and scaling: Accelerometer corruption was modeled as the combination of band-limited white noise, a constant bias, and a slowly varying bias random walk. The nominal accelerometer parameters were chosen to be representative of an automotive-grade MEMS IMU (MTi-1 class), and define the baseline case $s = 1$.

Suspension displacement sensing was corrupted using a bounded error model including linearity, repeatability, and quantization effects. The nominal parameters were selected to be representative of a compact linear displacement sensor (ILPS-19 class), and likewise define the baseline case $s = 1$.

A scalar factor

$$s \in \{0,\ 0.5,\ 1,\ 2,\ 4,\ 8,\ 16\}$$

was applied uniformly to the stochastic components of both noise models, with $s = 0$ denoting the noise-free case. For each scale, $N_{\mathrm{MC}} = 30$ trials were run using independent random seeds.

Results: Table VI summarizes the mean (μ) and standard deviation (σ) of the aggregate metrics over the N_{MC} trials. The mean aggregate RMSE and $P95$ remain nearly unchanged from $s = 0$ to $s = 8$, while the trial-to-trial dispersion increases steadily with noise scale. At the most severe level ($s = 16$), only a modest increase in mean error is observed. This indicates that the estimator is robust over a wide range

TABLE VI
AGGREGATE MONTE CARLO WHEEL-LOAD ERROR STATISTICS FOR INCREASING SENSOR-NOISE SCALE s (NÜRBURGRING SCENARIO). RESULTS ARE POOLED ACROSS ALL FOUR WHEELS.

s	RMSE$_\mu$ [N]	RMSE$_\sigma$ [N]	P95$_\mu$ [N]	P95$_\sigma$ [N]	Max$_\mu$ [N]	Max$_\sigma$ [N]
0	213.9	≈ 0	393.6	≈ 0	1778.8	≈ 0
0.5	213.9	0.31	393.6	0.50	1779.8	1.93
1	213.5	0.43	393.1	0.75	1779.1	3.02
2	214.0	1.30	393.6	2.14	1782.1	8.79
4	213.9	1.72	393.6	2.64	1783.8	10.90
8	214.2	4.10	394.2	6.13	1781.2	30.74
16	218.6	11.14	404.5	18.78	1805.0	50.23

of sensor-noise levels, with noise increasing trial-to-trial variability more than the mean error level.

This behavior is consistent with the two-stage estimator structure: suspension-based pseudo-measurements provide local wheel-resolved force information, while the soft rigid-body constraints regularize the four wheel-load estimates and preserve global physical consistency. Within the tested conditions, the results suggest that the dominant residual errors are due more to modeling mismatch and unmodeled dynamics than to sensor noise alone. The observed noise sensitivity is conditional on the adopted covariance tuning, particularly the pseudo-measurement covariance R_s and the constraint covariance R_c. While R_s determines how strongly suspension-measurement noise enters the first-stage update, R_c governs the extent to which the second-stage soft equilibrium constraints regularize those noisy per-corner estimates. Accordingly, the present Monte Carlo study should be interpreted as characterizing the estimator under the nominal (R_s, R_c) tuning used in this work, rather than as a tuning-independent property.

G. Summary of validation findings

The validation results demonstrate a clear hierarchy of contributions. The physics-constraint update constitutes the primary source of robustness by enforcing global physical consistency in the wheel-load distribution. Anti-roll-bar coupling and aerodynamic compensation provide additional accuracy improvements, while damper asymmetry has a comparatively minor influence under the evaluated conditions.

Collectively, these findings confirm that the proposed estimator offers a balanced combination of local suspension sensitivity and global physical consistency, making it well suited for real-time deployment in advanced chassis control systems.

V. CONCLUSION

This paper presented a physics-constrained Kalman filtering framework for estimating individual wheel normal loads using suspension and IMU measurements. The method combines suspension-based wheel-load pseudo-measurements with IMU-based soft rigid-body equilibrium constraints, allowing the estimator to retain local sensitivity to suspension-induced load variations while enforcing global physical consistency in the wheel-load distribution within a simple and modular structure. Aerodynamic vertical-load effects were also incorporated into the equilibrium constraints to reduce speed-dependent bias at higher vehicle speeds.

Validation in IPG CarMaker across an ISO double lane change and full-lap Nürburgring and Hockenheim scenarios showed that the proposed estimator provides the most consistent overall performance among the evaluated methods. In the ISO double lane change, the suspension-only reconstruction and stochastic observer remained highly competitive, reflecting the strong local suspension excitation of that maneuver. However, their full-lap performance was less competitive, whereas the proposed method delivered the strongest overall accuracy and robustness under broader combined-excitation conditions. Ablation studies showed that the physics-constraint update is the primary contributor to robustness, with anti-roll-bar coupling and aerodynamic compensation providing additional gains. Structural comparisons based on the Cheon benchmark further supported the value of the global constraint update, and Monte Carlo analysis indicated robustness over a wide range of sensor-noise levels under the nominal covariance tuning used in this work.

Overall, the proposed method provides a computationally lightweight and extensible framework for online wheel normal-load estimation. The present results are based on simulation validation in IPG CarMaker; future work will focus on experimental validation with real vehicle data, refinement of aerodynamic and suspension modeling, and extension to active-suspension and integrated chassis-control applications.

REFERENCES

[1] X. Ding, Z. Wang, L. Zhang, and J. Liu, "A comprehensive vehicle stability assessment system based on enabling tire force estimation," *IEEE Transactions on Vehicular Technology*, vol. 71, no. 11, pp. 11 571–11 588, 2022.

[2] Y. Liu, C. Huang, D. Zhou, X. Wang, and L. Li, "Vehicle sideslip angle estimation based on strong tracking SCKF considering road inclinations," *IEEE Transactions on Vehicular Technology*, vol. 72, no. 12, pp. 15 535–15 547, 2023.

[3] Z. Qin, L. Chen, M. Hu, and X. Chen, "A lateral and longitudinal dynamics control framework of autonomous vehicles based on multi-parameter joint estimation," *IEEE Transactions on Vehicular Technology*, vol. 71, no. 6, pp. 5837–5852, 2022.

[4] S. Tao, Z. Ju, L. Li, H. Zhang, and W. Pedrycz, "Tire road friction coefficient estimation for individual wheel based on two robust pmi observers and a multilayer perceptron," *IEEE Transactions on Vehicular Technology*, vol. 73, no. 9, pp. 12 530–12 541, 2024.

[5] Y. Wang, G. Yin, P. Hang, J. Zhao, Y. Lin, and C. Huang, "Fundamental estimation for tire road friction coefficient: A model-based learning framework," *IEEE Transactions on Vehicular Technology*, vol. 74, no. 1, pp. 481–493, 2025.

[6] M. Doumiati, A. Victorino, A. Charara, G. Baffet, and D. Lechner, "An estimation process for vehicle wheel-ground contact normal forces," *IFAC Proceedings Volumes*, vol. 41, no. 2, pp. 7110–7115, 2008.

[7] M. Doumiati, A. Victorino, D. Lechner, G. Baffet, and A. Charara, "Observers for vehicle tyre/road forces estimation: experimental validation," *Vehicle System Dynamics*, vol. 48, no. 11, pp. 1345–1378, 2010.

[8] J. Kun, A. Pavelescu, A. Victorino, and A. Charara, "Estimation of vehicle's vertical and lateral tire forces considering road angle and road irregularity," in *17th International IEEE Conference on Intelligent Transportation Systems (ITSC)*, 2014, Conference Proceedings, pp. 342–347.

[9] K. Jiang, A. C. Victorino, and A. Charara, "Adaptive estimation of vehicle dynamics through RLS and kalman filter approaches," in *2015 IEEE 18th International Conference on Intelligent Transportation Systems*, 2015, Conference Proceedings, pp. 1741–1746.

[10] Z. Ma, Y. Zhang, and J. Yang, "Velocity and normal tyre force estimation for heavy trucks based on vehicle dynamic simulation considering the road slope angle," *Vehicle System Dynamics*, vol. 54, no. 2, pp. 137–167, 2016.
[11] P. Luque, D. A. Mántaras, E. Fidalgo, J. Álvarez, P. Riva, P. Girón, D. Compadre, and J. Ferran, "Tyre–road grip coefficient assessment – part ii: online estimation using instrumented vehicle, extended kalman filter, and neural network," *Vehicle System Dynamics*, vol. 51, no. 12, pp. 1872–1893, 2013.
[12] D. Cheon, W. Choi, K. Nam, and S. Oh, "Tire normal force estimation based on integrated suspension state measurement," *International Journal of Control, Automation and Systems*, vol. 22, no. 6, pp. 1902–1911, 2024.
[13] R. A. Cordeiro, A. C. Victorino, P. A. V. Ferreira, E. C. de Paiva, and S. S. Bueno, "Tire-ground forces estimation in a 4-wheel vehicle using a delayed interconnected cascade-observer structure," *IFAC-PapersOnLine*, vol. 49, no. 15, pp. 139–144, 2016.
[14] R. A. Cordeiro, A. C. Victorino, J. R. Azinheira, P. A. V. Ferreira, E. C. d. Paiva, and S. S. Bueno, "Estimation of vertical, lateral, and longitudinal tire forces in four-wheel vehicles using a delayed interconnected cascade-observer structure," *IEEE/ASME Transactions on Mechatronics*, vol. 24, no. 2, pp. 561–571, 2019.
[15] V. A. Alatorre, A. Victorino, and A. Charara, "Estimation of wheel-ground contact normal forces: Experimental data validation," *IFAC-PapersOnLine*, vol. 50, no. 1, pp. 14 843–14 848, 2017.
[16] B. Ozkan, D. Margolis, and M. Pengov, "The controller output observer: Estimation of vehicle tire cornering and normal forces," *Journal of Dynamic Systems, Measurement, and Control*, vol. 130, no. 6, p. 061002, 09 2008.
[17] L. Filipozzi, F. Assadian, M. Kuang, R. Johri, and J. Velazquez Alcantar, "Estimation of tire normal forces including suspension dynamics," *Energies*, vol. 14, no. 9, p. 2378, 2021.
[18] A. H. Salari, H. Mirzaeinejad, and M. F. Mahani, "Tire normal force estimation using artificial neural networks and fuzzy classifiers: Experimental validation," *Applied Soft Computing*, vol. 132, p. 109835, 2023.
[19] L. Lu, G. Xu, and X. Chen, "Tire force estimation using model-based and machine learning approaches for distributed drive electric vehicle," in *CAA International Conference on Vehicular Control and Intelligence (CVCI)*, 2024, pp. 1–6.
[20] D. Meng, Y. Jiang, H. Chu, M. Tian, and B. Gao, "Data-driven tire forces estimation for autonomous vehicle applications," in *Chinese Control Conference (CCC)*, 2024, pp. 6421–6426.
[21] S. Öngir, E. C. Kaleli, M. Z. Konyar, and H. M. Ertunç, "Vertical force monitoring of racing tires: A novel deep neural network-based estimation method," *Applied Sciences*, vol. 15, no. 1, p. 123, 2025.
[22] X. Sun, T. Gu, Z. Quan, Y. Cai, H. Zhang, and B. Li, "Bayesian neural network-driven accelerometer-based type intelligent tire force measurement system," *Measurement*, vol. 253, p. 117699, 2025.
[23] Z. Tong, Y. Cao, R. Wang, Y. Chen, J. Xu, and S. Yang, "Intelligent tire force estimation with dynamic domain adaptation for varying wear states," *Mechanical Systems and Signal Processing*, vol. 241, p. 113526, 2025.
[24] Z. Quan, X. Sun, T. Gu, Y. Cai, H. Zhang, and X. Zhao, "A low-cost direct tire force measurement system using pvdf-integrated intelligent tires," *Measurement*, vol. 258, p. 119143, 2026.
[25] D. Simon and C. T. Li, "Kalman filtering with state equality constraints," *IEEE Transactions on Aerospace and Electronic Systems*, vol. 38, no. 1, pp. 128–136, 2002.
[26] C. V. Rao, J. B. Rawlings, and J. H. Lee, "Constrained linear state estimation—a moving horizon approach," *Automatica*, vol. 37, no. 10, pp. 1619–1628, 2001.
[27] N. Gupta and R. Hauser, "Kalman filtering with equality and inequality state constraints," 2007.
[28] D. Simon, "Kalman filtering with state constraints: a survey of linear and nonlinear algorithms," *IET Control Theory & Applications*, vol. 4, no. 8, pp. 1303–1318, 2010.
[29] N. A. Bouaynaya, G. Rasool, and C. Nidhal, "Constrained state estimation – a review," *arXiv eess*, 2022.
[30] M. Blundell and D. Harty, "Chapter 4 - modelling and analysis of suspension systems," in *The Multibody Systems Approach to Vehicle Dynamics*, second edition ed., M. Blundell and D. Harty, Eds. Oxford: Butterworth-Heinemann, 2015, pp. 185–334.
[31] J. Balkwill, "Chapter 8 - dynamic modelling of vehicle suspension," in *Performance Vehicle Dynamics*, J. Balkwill, Ed. Butterworth-Heinemann, 2018, pp. 241–317.
[32] P. S. Maybeck, *Stochastic Models, Estimation, and Control*. New York: Academic Press, 1979, vol. 1.
[33] D. Simon, *Optimal State Estimation: Kalman, H Infinity, and Nonlinear Approaches*. Hoboken, NJ: Wiley, 2006.
[34] T. D. Gillespie, *Fundamentals of Vehicle Dynamics*. Warrendale, PA, USA: SAE International, 1992.
[35] R. N. Jazar, *Vehicle Dynamics: Theory and Application*, 3rd ed. Cham, Switzerland: Springer, 2017.
[36] W.-H. Hucho, Ed., *Aerodynamics of Road Vehicles: From Fluid Mechanics to Vehicle Engineering*, 4th ed. Warrendale, PA, USA: SAE International, 1998.
[37] M. S. Grewal and A. P. Andrews, *Kalman Filtering: Theory and Practice with MATLAB*, 4th ed. Hoboken, NJ: Wiley, 2015.
[38] Infineon Technologies AG, *AURIX TC4x System Architecture*, Infineon Technologies AG, 2025, architecture overview.

BIOGRAPHY

Angus Siegloff Angus Siegloff is currently pursuing his bachelor's degree in electrical engineering with Federation University, Mt Helen, Australia. He has interned with the Terramechatronics Laboratory at Shibaura Institute of Technology, Saitama, Japan, and the Mobility Intelligence and Control Laboratory (MIC Lab) at the Korea Advanced Institute of Science and Technology (KAIST), Daejeon, South Korea.

Kyunghwan Choi Kyunghwan Choi received the B.S., M.S., and Ph.D. degrees in mechanical engineering from the Korea Advanced Institute of Science and Technology (KAIST), Daejeon, South Korea, in 2014, 2016, and 2020, respectively. He is currently an Assistant Professor with Cho Chun Shik Graduate School of Mobility, KAIST, and the Director of the Mobility Intelligence and Control Laboratory (MIC Lab). His research interests include vehicle dynamics and control, intelligent mobility systems, and autonomous vehicles.